ELSEVIER

Journal of Fluids and Structures 25 (2009) 954–966

JOURNAL OF FLUIDS AND STRUCTURES

www.elsevier.com/locate/jfs

A time-periodic approach for fluid-structure interaction in distensible vessels

B.W.A.M.M. Beulen*, M.C.M. Rutten, F.N. van de Vosse

Eindhoven University of Technology, Department of Cardiovascular Biomechanics, P.O. Box 513, 5600 MB Eindhoven, The Netherlands

Received 17 April 2008; accepted 27 March 2009
Available online 7 May 2009

Abstract

The analysis of periodic unsteady incompressible flow inside compliant vessels is of considerable interest for the simulation of blood flow in arteries. Weakly coupled fluid-structure interaction (FSI) models seem to be most suitable for this purpose. For weakly coupled solution methods, however, often convergence may not be achieved for compliant vessels with an axial length scale that is large compared to the characteristic radius. In this study, a time-periodic method for weakly coupled FSI models is presented. Approximate solutions of subsequent time-periods are obtained using the solution of the previous time-period as an initial solution. For the first period, not only suitable boundary conditions are derived from a 1-D wave propagation model, but also the initial axial pressure distribution. The time-periodic method was successfully applied to straight, curved and bifurcating geometries. The new approach proves to have a far better computational stability than weakly coupled methods based on timestep-wise coupling, especially in vessels with a length that is an order of magnitude larger than the radius.

Keywords: Hemodynamics; Weak coupling; Wave propagation; Time-periodic coupling

1. Introduction

Computational fluid dynamics (CFD) is a valuable tool for gaining insight into the hemodynamics of the vascular system. CFD models can be used to investigate the relationship between local hemodynamics and vascular (dys)function (Taylor et al., 1996), but can also be applied for improvement and validation of clinical measurement methods (Wolters et al., 2005).

In compliant complex geometries, 3-D FSI may provide accurate descriptions of deformation and flow phenomena. However, such models are very time consuming due to a high demand on computing resources. Consequently, 3-D computational methods are mostly applied to small segments of the arterial system (Taylor et al., 1998; Gijsen et al., 1999a, b; van de Vosse et al., 2003). The effects of the distal and proximal part of the section then need to be incorporated by means of proper boundary conditions, e.g. formulated in O.D.E.s of lesser geometrical scale, as in wave propagation (1-D) or lumped parameter (0-D) models. So, generally, the modelling of the fluid-structure interaction (FSI) of blood flow in arteries requires the combination of different types of models (Formaggia et al., 1999, 2001; Quarteroni and Veneziani, 2003; Fernandez et al., 2005), each with their own spatial dimensions (Fig. 1).

*Corresponding author.
E-mail address: b.w.a.m.m.beulen@tue.nl (B.W.A.M.M. Beulen).

0889-9746/$ - see front matter © 2009 Elsevier Ltd. All rights reserved.
doi:10.1016/j.jfluidstructs.2009.03.002

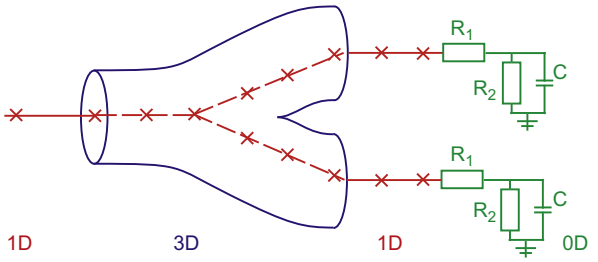

Fig. 1. Schematic representation of a geometric multi scale model.

Lumped parameter models, such as the Windkessel model, relate pressure to flow: $p(t) = p(q(t))$. A combination of lumped parameter models and 1-D wave propagation models may be applied for the global representation of the circulatory system (Olufsen et al., 2000). Wave propagation models are often applied to describe the propagation of pressure and flow waves through large sections of the arterial system (Hughes and Lubliner, 1973; Olufsen et al., 2000), requiring a significant smaller amount of computing resources than 3-D FSI models. These models can be utilised to provide the 2-D/3-D models with boundary conditions, either at the inlet or outlet (Vignon-Clementel et al., 2006), but also on a larger section of the model (Reuderink et al., 1993).

Mathematically, FSI models are based on the 3-D Navier–Stokes equations, describing the fluid motion, and the equations of motion for solids describing the vessel wall (structure) motion and deformation. A coupling has to be implemented between the fluid problem and the solid problem by means of dynamic and kinematic interface conditions. The pressure and shear load from the fluid side of the fluid–solid interface has to be in equilibrium with the traction at the boundary of the solid at the fluid–solid interface (dynamic interface condition). In addition, the velocity of the solid must equal the fluid velocity at the fluid–solid interface (kinematic interface condition).

In fully coupled solution methods, the fluid and the solid problem are solved simultaneously (de Hart et al., 2003; van Loon et al., 2004; Giannopapa, 2004). Typically, in arterial FSI problems, the eigenvalues of the system matrices associated with both problems are more than nine orders of magnitude apart, resulting in a badly conditioned total matrix for the total system. Consequently, these methods can be computationally expensive and require large computer resources.

In partitioned FSI approaches (Matthies and Steindorf, 2002), the fluid and the solid problem are solved sequentially, using standard methods for both domains. The fluid and solid problems are then coupled through the interface conditions described above.

In decoupled solution methods, the fluid and solid problem are solved independently. In the case that the wavelength of the pressure pulse travelling through the vessel is large compared to the section of interest, the pressure distribution inside the vessel may be assumed spatially constant and can be chosen equal to the prescribed outlet pressure, which e.g. can be determined from a 0-D or 1-D model. For arteries with a large length-to-radius ratio, this decoupled procedure may be inadequate due to a non-negligible axial pressure drop. 1-D models, however, can also be applied to prescribe the pressure distribution inside the vessel (Reuderink et al., 1993). Although this approximation can be more appropriate, it becomes inaccurate for the case that the 1-D model is incapable to adequately represent the pressure gradients due to complex flow phenomena (e.g. in complex geometries).

For arterial FSI problems, partitioned schemes are preferred. A partitioned approach is likely to be feasible because the flow-induced pressure variations, being in the order ρV^2, are an order in magnitude smaller than the amplitude of the pressure wave travelling through the arterial system. So, inaccuracies in the velocity field will hardly influence the wall motion. In partitioned schemes, weakly and strongly coupled approaches exist.

In weakly coupled methods, the flow-induced pressure is transferred timestep-wise to the solid as a normal stress at the fluid–solid interface. This induces the wall motion. Only one solution of solid and fluid problem is required per time step, making it appealing in terms of computational effort. Two problems, typical for weakly coupled methods, may arise. First, in the weakly coupled approach no convergence may be achieved due to the so-called added mass effect, which has been analysed by amongst others Forster et al. (2007) and Causin et al. (2005), and is found to be dependent on the density/mass ratio between solid and fluid. However, in specific cases, it can be justified to employ a quasi-stationary approach for modelling the solid, averting convergence problems related to the added mass effect (Section 2.1.2). A second problem that may arise is that the solution of the fluid problem is always one step behind of the solution of the solid problem. Due to the phase error between fluid and solid computation, a temporal computational instability, which cannot be avoided by refinement of the spatial and temporal discretisation, can occur. For tubes with a high length-to-radius ratio this can lead to errors in the total volume of the domain considered that are

of equal order as the flow flux during a single time step (Rutten, 1998), causing the method not to converge, either due to divergence of the fluid or solid computation.

In general, convergence issues in partitioned schemes can be overcome by strongly coupled methods, which apply sub-iterations and under relaxation for solution of the solid and fluid problem for each time step to converge to the solution of the fully coupled system (Fernandez et al., 2006; Fernandez and Moubachir, 2005; Deparis et al., 2006). The major drawback of these kinds of methods are non-robustness and the increasing amount of computational costs.

An alternative partitioned scheme is based on sequential coupling, as applied in the SCAFSI method, which was recently introduced by Tezduyar et al. (2008a, b). Test computations performed on cerebral and abdominal aortic aneurysm geometries showed improved convergence properties, without requiring a significant increase in computational demand.

In this study, a similar time-periodic approach for weakly coupled 3-D FSI is presented, which enables the modelling of time-periodic incompressible flow inside clinically relevant compliant geometries, i.e. straight and weakly curved vessels, with a high length-to-radius ratio, and bifurcations.

The second section of this paper starts with an overview of the equations, which describe the flow of an incompressible fluid through a compliant vessel and the deformation and motion of the vessel wall (Section 2.1). Next, a description of the time-periodic coupling method, as proposed in this study, is given in Section 2.2. The implementation of the models in the computational framework is discussed in Section 2.4. In Section 2.5, a series of simulations is presented, which is used to study the convergence properties of the time-periodic coupling method. The results of this analysis are presented in Section 3. Finally, two applications of FSI-computations are presented in Section 4. The discussion and conclusions are given in Sections 5 and 6.

2. Materials and methods

2.1. The 3-D model

Consider a spatial domain Ω and its boundary Γ as illustrated in Fig. 2. The spatial domain is subdivided into a fluid domain, Ω_f, with boundary Γ_f, subdivided into Γ_{fi}, Γ_{fo} and Γ_{fs} and a solid domain, Ω_s, with boundary Γ_s, subdivided into Γ_{si}, Γ_{so} and $\Gamma_{sf}=\Gamma_{fs}$. The boundary that separates the fluid and the solid domain is indicated by Γ_{fs}.

The blood velocity and pressure distribution in the vessel are computed by solving the Navier–Stokes equations on the deforming fluid domain Ω_f based on the arbitrary Lagrangian–Eulerian (ALE) method (Donea et al., 1982). The displacements in the vessel wall are computed by solving the equations of motion and continuity on the solid domain Ω_s.

2.1.1. Blood flow

Denoting the fluid velocity by $\mathbf{v}(\mathbf{x},t)$ (with $\mathbf{x}\in\Omega_f, t>0$), the pressure by $p(\mathbf{x},t)$ and the constant fluid density by ρ, the ALE formulation of the Navier–Stokes equation for an incompressible fluid reads:

$$\begin{aligned} &\rho\frac{\partial \mathbf{v}}{\partial t}\bigg|_{\Omega(t)} + \rho(\mathbf{v}-\mathbf{w})\cdot\nabla\mathbf{v} - \nabla\cdot\boldsymbol{\sigma} - \mathbf{f} = \mathbf{0} \quad \text{in } \Omega_f,\\ &\nabla\cdot\mathbf{v} = \mathbf{0} \qquad\qquad\qquad\qquad\qquad\qquad\quad \text{in } \Omega_f, \end{aligned} \tag{1}$$

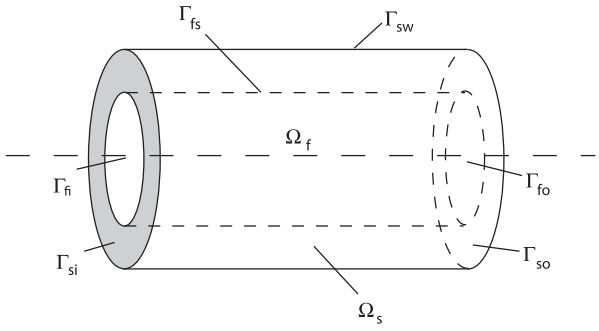

Fig. 2. Simple compliant tube.

with $\boldsymbol{\sigma}$ the Cauchy stress tensor, $\mathbf{w}$ the velocity of the fluid domain and $\mathbf{f}$ the external body forces per unit of volume. In this study the body forces are assumed to be zero; for example, influences of gravity are neglected. The time derivative is defined with respect to the moving grid. Considering blood as a Newtonian fluid, the Cauchy stress tensor is defined as

$$\boldsymbol{\sigma} = -p\mathbf{I} + 2\eta\mathbf{D}, \tag{2}$$

with p the fluid pressure, η the viscosity $\mathbf{I}$ the identity tensor and $\mathbf{D} = \frac{1}{2}(\nabla\mathbf{v} + (\nabla\mathbf{v})^{\mathrm{T}})$ the rate of deformation tensor.

For the boundary conditions, at the inflow boundary, Γ_{fi}, a Womersley velocity profile $v_n(\mathbf{x}, t)$ corresponding to a flow $q_i(t)$ is prescribed in the normal direction. At the outflow boundary, Γ_{fo}, the normal stress is prescribed in terms of a given pressure, $p_o(t)$, and at the fluid/solid boundary a no-slip condition is prescribed, the fluid velocity is equal to the grid velocity $\mathbf{w}$

$$\begin{aligned} &\mathbf{v} - \mathbf{w} = v_n(\mathbf{x}, t)\mathbf{n} && \text{on } \Gamma_{fi}, \\ &\boldsymbol{\sigma}\cdot\mathbf{n} = p_o\mathbf{n} && \text{on } \Gamma_{fo}, \\ &\mathbf{v} = \mathbf{w} && \text{on } \Gamma_{fs}, \end{aligned} \tag{3}$$

with $\mathbf{n}$ being the outward boundary normal. For more detailed information on the equations applied, we refer the reader to van de Vosse et al. (2003).

2.1.2. Wall deformation

The displacements in the vessel wall, $\mathbf{u}$, are computed by solving the equations of motion (with no body forces) and continuity on the solid domain Ω_s:

$$\rho\frac{\partial^2\mathbf{u}}{\partial t^2} + \nabla\cdot\boldsymbol{\sigma} = \mathbf{0} \quad \text{in } \Omega_s, \quad \det(\mathbf{F}) - 1 = 0 \quad \text{in } \Omega_s, \tag{4}$$

with $\boldsymbol{\sigma}$ the Cauchy stress tensor and $\mathbf{F} = (\nabla_0\mathbf{x}(t))^{\mathrm{T}}$ the deformation gradient tensor defining the deformation between the reference state Ω_0 and the current state $\Omega(t)$.

The vessel wall is considered a linearly elastic neo-Hookean material for which the Cauchy stress tensor is defined by

$$\boldsymbol{\sigma} = -p\mathbf{I} + G(\mathbf{B} - \mathbf{I}), \tag{5}$$

with p the hydrostatic pressure, $\mathbf{I}$ the unit tensor, G the shear modulus and the Finger tensor $\mathbf{B}$, defined as $\mathbf{B} = \mathbf{F}\cdot\mathbf{F}^{\mathrm{T}}$. The shear modulus is assumed to be constant. Also other, non-linear, material behaviour can be used without loss of generality.

Under the assumption that the vessel wall thickness, h, is small compared to the vessel radius, a_0, the momentum equation in radial direction reduces to

$$\rho h\frac{\partial^2 u_r}{\partial t^2} = p - \frac{\sigma_{\vartheta\vartheta}h}{a_0}. \tag{6}$$

The left hand side of equation (6) can be approximated by

$$\rho h\frac{\partial^2 u_r}{\partial t^2} \approx \rho h\omega^2 u_r = \mathcal{O}(10^{-4}\,\mathrm{Pa}). \tag{7}$$

For arteries, the internal pressure is typically of $\mathcal{O}(10^4\,\mathrm{Pa})$. Therefore the inertial term in the momentum Eq. (4) may be neglected: circumferential stresses, $\sigma_{\vartheta\vartheta}$, are balanced by the internal (transmural) pressure p. A quasi-stationary approach is applied for modelling the solid.

At the cross-sectional surfaces at the inflow and the outflow boundaries, Γ_{si} and Γ_{so}, respectively, all displacements are constrained. At the fluid/solid boundary, the pressure and shear load from the fluid is applied as a traction boundary condition for the solid. For convenience, the shear load will be neglected in this study, since for the intended application, the influence of shear forces is negligible. So, at the fluid/solid boundary, Γ_{fs}, the normal stress is prescribed in terms of a given pressure load, p_w. The outer wall boundary, Γ_{sw}, is considered stress free in normal direction:

$$\begin{aligned} &\mathbf{u} = \mathbf{0} && \text{on } \Gamma_{si}\cup\Gamma_{so}, \\ &\boldsymbol{\sigma}\cdot\mathbf{n} = -p_w\mathbf{n} && \text{in } \Gamma_{fs}, \end{aligned} \tag{8}$$

again with $\mathbf{n}$ the outward boundary normal.

2.1.3. Grid motion

The velocity of the fluid mesh, $\mathbf{w}$, is determined by solving a linear elastic deformation of a compressible solid problem defined on the fluid domain, where the displacement of the wall is used as an essential boundary condition in Γ_{fs} and where the displacement in Γ_{fi} and Γ_{fo} equals zero. By choosing the finite element space for this linear elastic problem equal to the one used for the fluid solver, isoparametric elements are ensured for all time steps.

2.2. Time-periodic weak coupling

In this study, the existing decoupled and weakly coupled methods for FSI are compared to the newly introduced time-periodic coupling method. In the time-periodic approach, the flow-induced pressures are transferred time period-wise to the solid. This is allowed, as long as periodic functions are applied as boundary conditions, and the solution is assumed to be periodic accordingly. The algorithm is as follows.

Given a pressure $p_{k-1}(\mathbf{x}, t)$ on the time interval $[kT, (k+1)T]$, for each time-step t_n in the time interval $[kT, (k+1)T]$:

(i) solve the solid problem to find the displacement $\mathbf{u}_k(\mathbf{x}, t_n) = \mathbf{u}(p_{k-1}(\mathbf{x}, t_n))$,
(ii) calculate the grid velocity, $\mathbf{w}_k(\mathbf{x}, t_n)$, of the fluid domain,
(iii) solve the fluid problem to find the velocity, $\mathbf{v}_k(\mathbf{x}, t_n)$, and pressure distribution, $p_k(\mathbf{x}, t_n)$.

The algorithm continues until $p_k(\mathbf{x}, t)$ converges to a limit function $p(\mathbf{x}, t)$ within a predefined tolerance. The algorithm is initiated with the pressure distribution obtained from a 1-D wave propagation model, which also provides the boundary conditions for the fluid problem.

For the weakly coupled method, the flow-induced pressure are transferred timestep-wise to the solid: $\mathbf{u}_k(\mathbf{x}, t_n) = \mathbf{u}(p_k(\mathbf{x}, t_{n-1}))$. Again, the boundary conditions for the fluid problem are provided by the 1-D wave propagation model. For the decoupled method, not only the boundary conditions are derived from the wave propagation model, but also the axial pressure distribution which drives the wall motion: $\mathbf{u}_k(\mathbf{x}, t_n) = \mathbf{u}(p_{1D}(x, t_n))$.

2.3. 1-D model

For the 1-D approximations, the time-domain based wave propagation model as introduced by Bessems et al. (2007) is applied. Contrary to present models (Stergiopulos et al., 1999; Formaggia et al., 2001), this model allows phase differences between the boundary layer flow and the flow inside the inviscid core of the vessel. This results in proper estimates for the friction and non-linear term in the momentum balance (Bessems et al., 2007), providing an accurate description of wave propagation (Bessems et al., 2008).

At the outlets of the 1-D model, three-element Windkessel models, with parameters R_1, R_2 and C_T (Fig. 1), are defined to relate the outlet pressure to outlet flow (Stergiopulos et al., 1999). The value of the terminal resistance, R_1, is obtained by modelling minimal reflections at the outlets

$$R_1 \sim Z_0 = \sqrt{\frac{L_0}{C_0}} = \sqrt{\frac{\rho h E}{2\pi^2(1-\nu^2)a_0^5}}, \tag{9}$$

with $L_0 = \rho/a_0$ representing the local inertance, C_0 the local compliance and Z_0 the local impedance at the distal end of the vessel. The vessel wall thickness and radius are, respectively, denoted by h and a_0, E is Young's modulus, ν is the Poisson ratio and ρ is the fluid density. The peripheral resistance, R_2, and the compliance, C_T, are adjusted such that pressures within the physiological range are obtained and a physiological pressure drop is achieved

$$R_1 + R_2 = \frac{\bar{p}}{\bar{q}} \quad \text{and} \quad C_T = \tau/R_2, \tag{10}$$

in which $\bar{p}$ is the desired mean pressure and $\bar{q}$ is the mean flow prescribed at the inlet. The time constant $\tau = 1.5\,\text{s}$ was found to result in a physiological pressure drop.

2.4. Implementation

The 1-D wave propagation model is applied to a 1-D mesh representing the centreline of the geometry considered. Locally, at a smaller section of the 1-D model, a 3-D computational domain is defined at which the 3-D FSI model is implemented. The equations from both models are solved successively.

To solve the equations resulting from the 1-D wave propagation model a spectral element method is employed, as described by Bessems et al. (2007). This results in a solution for the pressure, $\hat{p}(\xi, t)$, and the flow, $\hat{q}(\xi, t)$, in each node, ξ_i, of the 1-D mesh, $1 \leqslant i \leqslant N$. N is the total number of nodes in the 1-D mesh.

To apply the pressure distribution from the 1-D model to the 3-D section, the pressure at the fluid–solid interface is set equal to the pressure at the nearest point at the centreline, for each node at the fluid–solid interface. The pressure at the points at the 3-D centreline is determined from the 1-D solution using a linear interpolation (Fig. 3). The linear interpolation results in $\hat{p}(\boldsymbol{\psi}_c, t)$ and $\hat{q}(\boldsymbol{\psi}_c, t)$, on which the points at the 3-D centreline are indicated by $\boldsymbol{\psi}_c = (\psi_1, \ldots, \psi_M)$. At the entrance of the 3-D segment, the flow is prescribed according to $q(\psi_{\text{in}}) = \hat{q}(\xi_{\text{in}})$, at the exit, the normal stress is prescribed according to $(\boldsymbol{\sigma} \cdot \mathbf{n})_{\text{out}} = \hat{p}(\xi_{\text{out}})\mathbf{n}$.

For bifurcating geometries, it is assumed that the pressure gradients within the centre section are negligibly small, such that in the centre section of the 3-D bifurcation, a uniform pressure, equal to the pressure in the 1-D bifurcation can be prescribed.

In the 3-D FSI model a first order Euler-implicit discretisation scheme is used for temporal discretisation of the equations presented in Section 2.1. The equations are consecutively linearised using the Newton–Raphson method, discretised and solved on a mesh consisting of 27-noded, isoparametric tri-quadratic Crouzeix–Raviart hexahedrons using the SEPRAN finite element package (Segal, 2004).

2.5. Convergence analysis

An idealised model of the common carotid artery (CCA) is used to study the time-periodic approach. The CCA geometry is modelled as a straight vessel with a radius of $a_0 = 3\,\text{mm}$ and a wall thickness of $h = 0.5\,\text{mm}$. The value of the shear modulus G of the wall is prescribed to be 300 kPa. This value is chosen such that the maximum of the radial deformation for the physiological pressure range is approximately 5% (Milnor, 1989). For the blood flow a Newtonian fluid is used with a density of $1.06 \times 10^3\,\text{kg m}^{-3}$ and a dynamic viscosity of $4.9 \times 10^{-3}\,\text{kg m}^{-1}\text{s}^{-1}$.

At the inlet of the 1-D model a smooth waveform resembling CCA flow is prescribed. The outlet of the 1-D model is terminated by a three-element Windkessel model, with parameters $R_1 = 3.6 \times 10^{12}\,\text{kg m}^{-4}\,\text{s}$, $R_2 = 8.6 \times 10^{12}\,\text{kg m}^{-4}\,\text{s}$ and $C_T = 1.2 \times 10^{-13}\,\text{m}^4\,\text{s}^2\,\text{kg}^{-1}$. In Fig. 4, the prescribed flow waveform and the resulting pressure waveform at the exit of the 1-D model are presented.

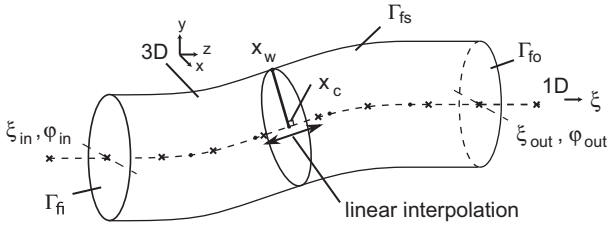

Fig. 3. Schematic overview of the 1-D and 3-D domain. The × indicates 1-D nodes and the • indicates 3-D centreline nodes. For each node located at the fluid–solid interface, for example x_w, the nearest point located at the centreline, indicated by x_c, is determined. The pressure in x_w is set equal to the pressure in x_c, which is determined from the 1-D pressure by a linear interpolation.

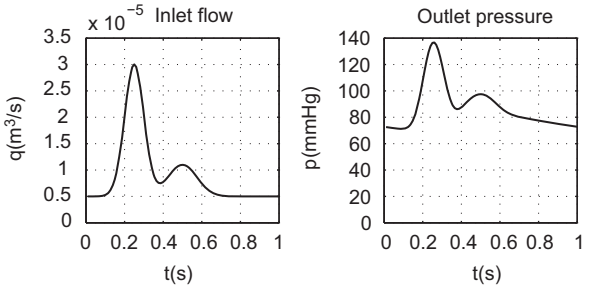

Fig. 4. At the left, the flow waveform prescribed at the inlet of the 1-D model is shown. The resulting pressure waveform at the outlet of the 1-D model is shown at the right.

For the input flow, with geometrical and fluid properties as shown above, the Reynolds number, defined as $\mathrm{Re} = \rho v a_0/\mu$, ranges from 100 to 800, which is in the physiological relevant range (Ku, 1983).

The geometry described above is defined at $p = 0$ mmHg. Before the FSI calculations are initiated the pressure load on the wall is slowly increased toward diastolic pressure level. This prevents a sudden wall motion, due to a large pressure step, at the first time step.

To study the convergence properties of the time-periodic approach, an FSI-computation has been performed for $t \in [0, 5T]$ on a section of the CCA with a length $L = 40a_0$. A discrete L_2-norm is applied to determine the convergence rate

$$\varepsilon = \|\bar{p}_{n+1} - \bar{p}_n\|_2 = \sqrt{\sum_i (\bar{p}^i_{n+1} - \bar{p}^i_n)^2}, \tag{11}$$

in which the nodes in the fluid domain are indicated by i. $\bar{p}_n$ Is the mean value of the pressure solution from the 3-D Navier–Stokes equation, during period n.

To compare the performance of the time-periodic, decoupled and weakly coupled methods, FSI-computations were performed for vessel geometries with increasing length-to-radius ratio ($L/a_0 = 10, 20, 40, 50$ and 60). Convergence of inlet pressure (p_i) and outlet flow (q_o) solutions of the decoupled and time-periodic method are compared by means of the discrete L_2-norm

$$\varepsilon_q = \left\| \frac{q_{o,dc} - q_{o,tp}}{q_{o,tp}} \right\|_2 \quad \text{and} \quad \varepsilon_p = \left\| \frac{p_{i,dc} - p_{i,tp}}{p_{i,tp}} \right\|_2, \tag{12}$$

in which the subscripts dc and tp, respectively, indicate the decoupled and time-periodic approach.

3. Results

The results of the convergence analysis are presented in Fig. 5. They clearly show a monotonic decrease of the residual ε with increasing period number n. All pressure and flow solutions presented in the remainder of this study were obtained by performing computations for five periods (for $n = 4$, $\varepsilon = \mathcal{O}(10^{-4})$).

It was found that the weakly coupled approach is applicable to vessels up to $L/a_0 \approx 10$, for vessels of higher length the computations diverge. The time-periodic and the decoupled methods are successfully applied to vessels up to $L/a_0 = 60$. No significant differences with respect to computation time and convergence between both methods were found, which is to be expected, since for both methods equal solution methods are applied and only minor differences in prescribed boundary conditions exist.

In Fig. 6 the results of the FSI-computations for the inlet/outlet flow and inlet/outlet pressure, for the straight section of $L = 20a_0$ and $50a_0$ of the CCA are presented. For each calculation method, respectively, the inlet flow and the outlet

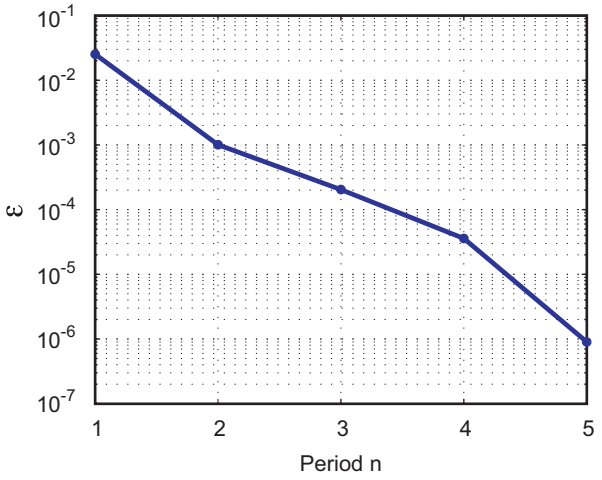

Fig. 5. Convergence analysis applied on the pressure solution of a time-periodic FSI-computation performed on a straight section of the CCA with a length $L = 40a_0$.

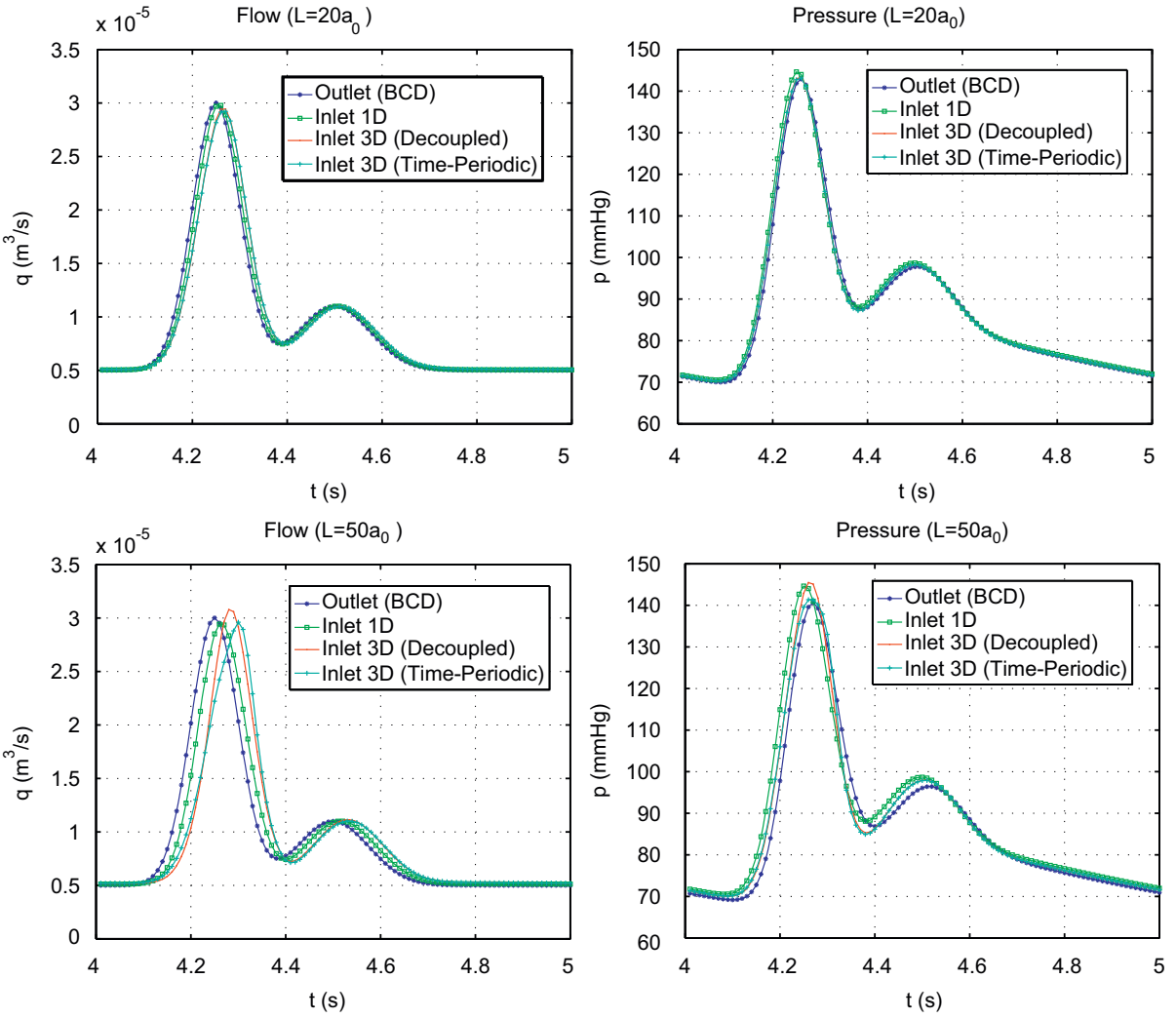

Fig. 6. Results of the FSI-computations for the inlet/outlet flow and inlet/outlet pressure calculated by the 1-D model, the decoupled approach and the time-periodic approach for straight sections of the CCA with a length of $L = 20a_0$ and $50a_0$.

pressure are equal since these are the imposed boundary conditions. Generally, for short sections ($L = 20a_0$) minor differences ($\varepsilon_q = 3 \times 10^{-2}$, $\varepsilon_p = 3 \times 10^{-3}$) occur, whereas for longer sections ($L = 50a_0$), more significant differences ($\varepsilon_q = 4 \times 10^{-1}$, $\varepsilon_p = 1 \times 10^{-1}$) in solution are found between the decoupled and time-periodic approach.

Deviations between 1-D and 3-D flow and pressure solutions are present which can be caused by the difference in solid model applied for the 1-D and 3-D computations. A closer analysis of the wall motion shows a maximum difference of 2% in wall distension between 1-D and 3-D model, which indicates that the 3-D solution offers a sensible solution for the FSI problem.

4. Applications

In vivo, the CCA and most other arteries are not straight, but have a significant curvature. MR and ultrasound imaging studies of CCA morphology have shown that the ratio of curvature, δ ($\delta = a_0/R$), for the CCA can range up to 3% (Tortoli et al., 2003). Fluid flowing through a curved vessel experiences a centripetal force. The fluid in the core of the tube is forced towards the outside of the bend, which results in secondary flows and thus an energy loss. Therefore,

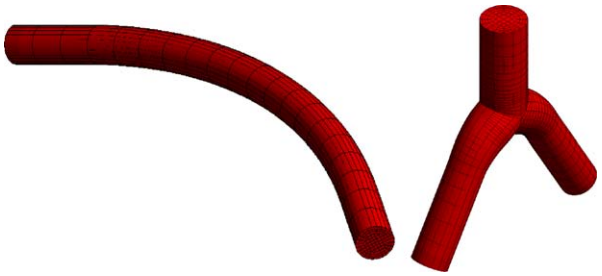

Fig. 7. Left: geometry for the curved section of the CCA and right: the carotid bifurcation.

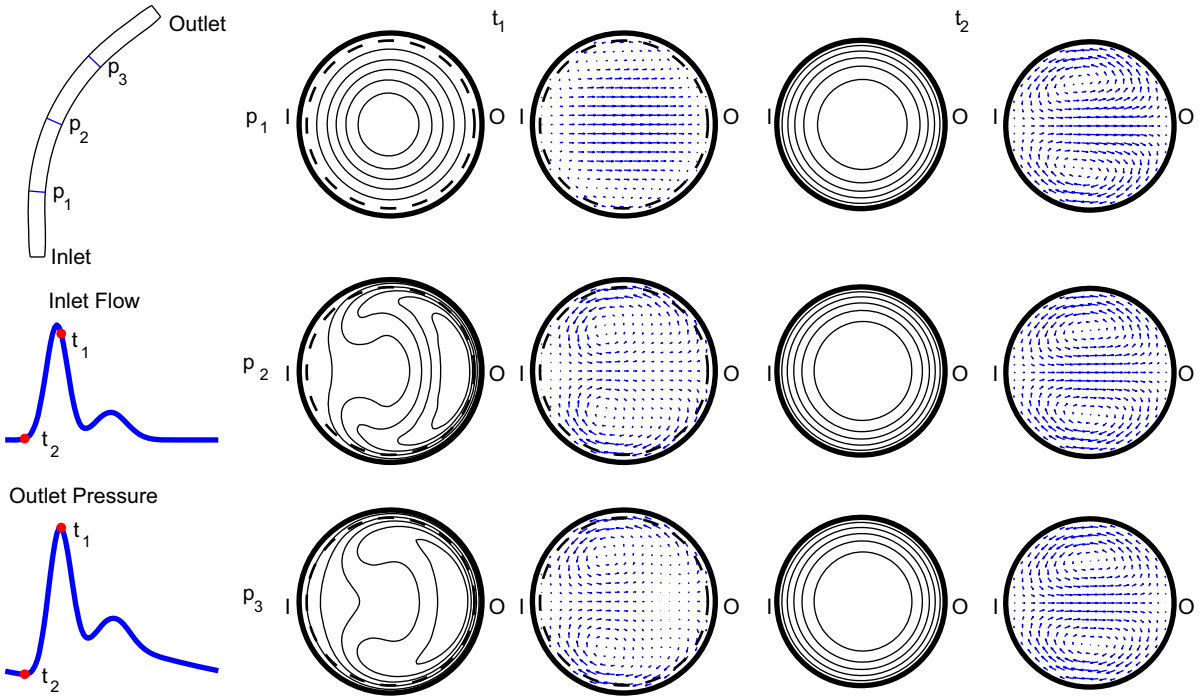

Fig. 8. Results of the time-periodic FSI-simulation performed on the curved vessel. The flow field is visualised at three positions (p_1, p_2 and p_3) at peak systolic time t_1 and end diastolic time t_2. The contour plots show the axial velocity distribution, the vector plots show the secondary velocity profiles, I denotes the inside of the bend, O denotes the outside, the dashed line indicates the position of the vessel wall at the end diastolic time.

the axial pressure drop in a curved tube is larger than the pressure drop in a straight tube of equal length (Dean, 1928). Besides an axial pressure gradient, also cross-sectional pressure gradients are present: the pressure-load distribution on the vessel wall is non-uniform due to 3-D flow phenomena. Furthermore, the arterial tree is a highly bifurcating network. As in curved vessels, also in bifurcations, non-uniform pressure-load distributions occur, possibly influencing the wall motion.

For both curved and bifurcating geometries, the performance of the time-periodic coupling method is compared to the performance of the decoupled approach.

For the curved geometry, a curved section of the CCA with a length of $40a_0$ and a curvature ratio of 3% is considered (Fig. 7). For vessel properties and boundary conditions, equal values as presented in Section 2.5 are applied.

For the bifurcating geometry, the carotid bifurcation is modelled as an idealised symmetric planar bifurcation (Fig. 7). The inlet trunk of the bifurcation has a radius of 3 mm, and a length of $L_i = 4a_0$. The radius of the outlet trunk is chosen such that the average shear rate at the outlet is equal to the average shear rate at the inlet, the length of the outlet trunks is equal to $L_o = 8a_0$. The angle between both outlet trunks is 120°.

At the inlet of the 1-D bifurcation model a smooth flow waveform, resembling the CCA flow is prescribed. At the outlets, the 1-D model is terminated by a three-element Windkessel model, with parameters $R_1 = 6.5 \times 10^{12}\,\mathrm{kg\,m^{-4}\,s}$, $R_2 = 8.2 \times 10^{11}\,\mathrm{kg\,m^{-4}\,s}$ and $C_T = 1.8 \times 10^{-14}\,\mathrm{m^4\,s^2\,kg^{-1}}$ (Eqs. (9) and (10)).

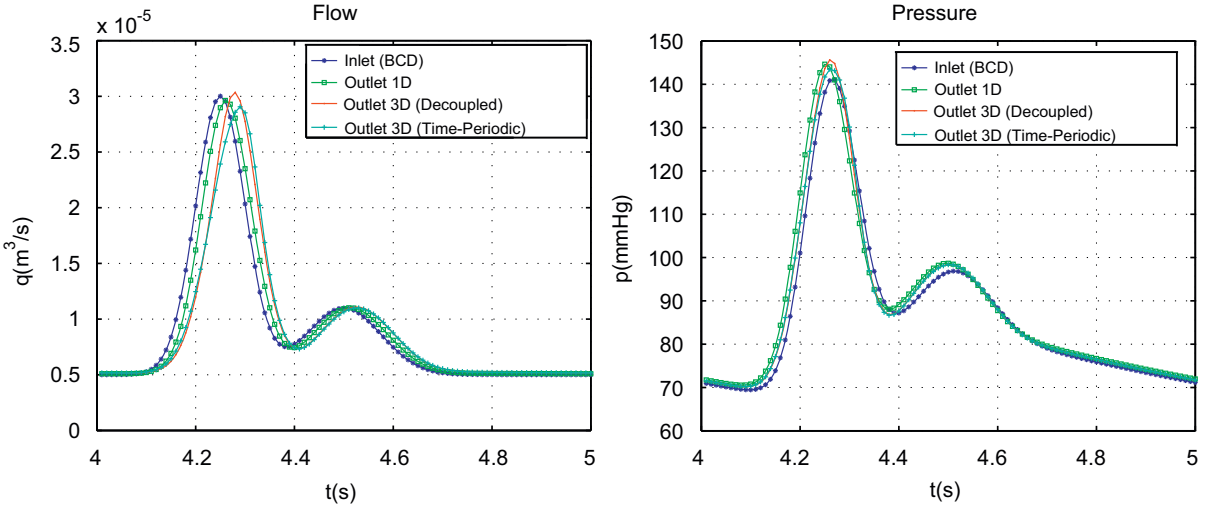

Fig. 9. Results of the FSI-computations for the inlet/outlet flow and the inlet/outlet pressure calculated by the 1-D model, the decoupled approach and the time-periodic approach for the curved section of the CCA.

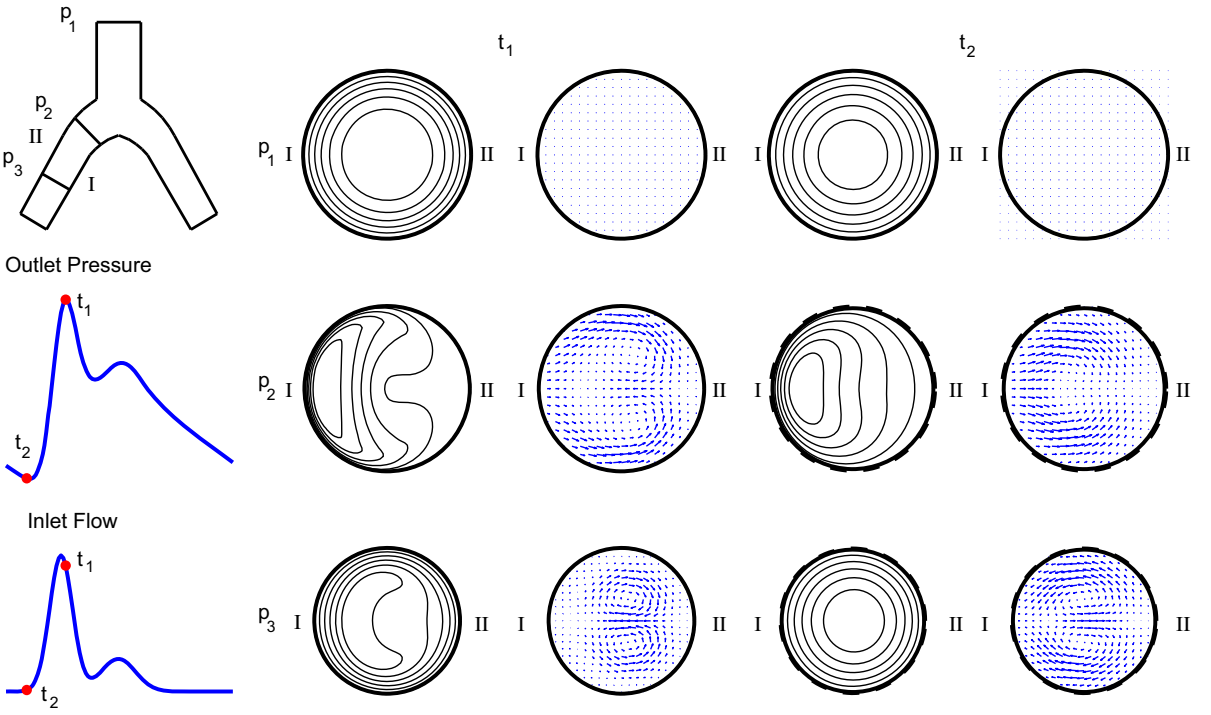

Fig. 10. Results of the time-periodic FSI-simulation performed on the bifurcation. The flow field is visualised at three positions (p_1, p_2 and p_3) at peak systolic time t_1 and end diastolic time t_2. The contour plots show the axial velocity distribution, the vector plots show the secondary velocity profiles, I and II indicate the orientation of the plane with respect to the bifurcation.

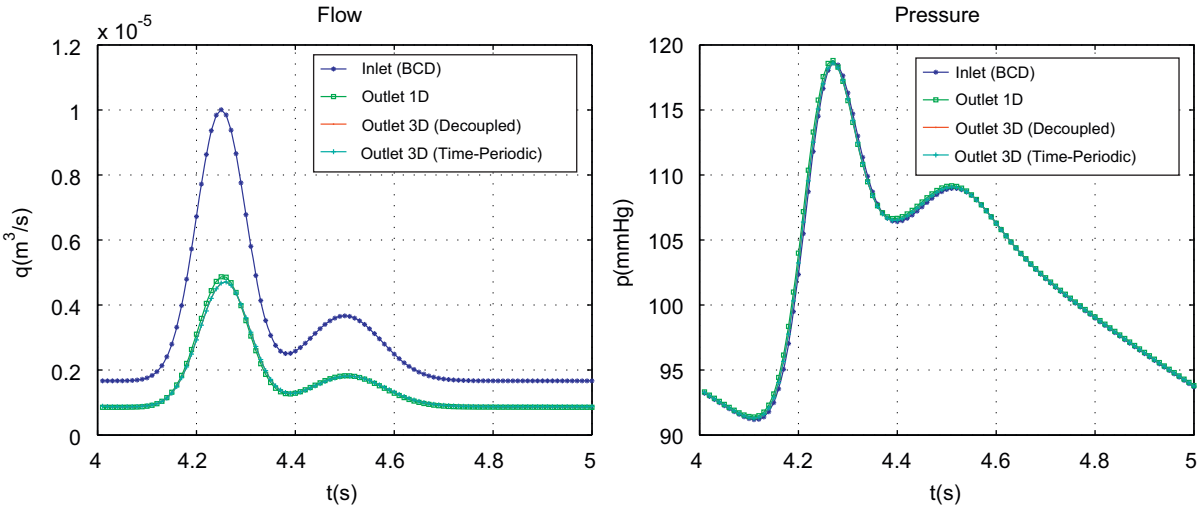

Fig. 11. Results of the FSI-computations for the inlet/outlet flow and the inlet/outlet pressure calculated by the 1-D model, the decoupled approach and the time-periodic approach for the bifurcation geometry.

The flow field in the curved vessel geometry, as calculated using the time-periodic coupling method clearly shows the development of the asymmetric axial velocity distribution and the presence of the secondary velocity field (Fig. 8). For the decoupled and time-periodic approach, a comparison (Fig. 9) of the inlet/outlet flow and inlet/outlet pressure, indicates deviations between 1-D and 3-D flow and pressure solutions, which can be caused by the difference in the solid model applied for the 1-D and 3-D computations. Differences between decoupled and time-periodic coupling method are found to be $\varepsilon_q = 2 \times 10^{-1}$ and $\varepsilon_p = 4 \times 10^{-2}$.

For the bifurcating geometry, the flow field calculated using the time-periodic coupling method is presented in Fig. 10. In the outlet trunks, the characteristic asymmetric axial velocity distribution and secondary velocity field are clearly visible. In Fig. 11 the results of the FSI-computations for the inlet/outlet flow and inlet/outlet pressure for the carotid bifurcation are presented. The graphs in Fig. 11 show no significant differences between 1-D and 3-D, furthermore, also no significant differences ($\varepsilon_q = 5 \times 10^{-6}$, $\varepsilon_p = 7 \times 10^{-8}$) in solution arise for the decoupled and time-periodic coupling method.

5. Discussion

The weakly coupled time-periodic FSI method is successfully applied to straight, curved and bifurcating geometries. Approximate solutions of the pressure distribution of subsequent time-periods are obtained using the pressure solution of the previous time step as an initial condition. Contrary to most present models, 1-D models are not only applied for supplying boundary conditions, but also as an approximation for the initial axial pressure distribution inside the 3-D section. The convergence analysis shows good results, but since no theoretical results are available for the time-periodic approach, no comparison with literature can be made. Additionally, it should be noted that the proposed algorithm is not suitable for transient analysis, since it is based on the assumption that periodic functions are applicable for the boundary conditions.

The time-periodic coupling method has been compared to the decoupled and weakly-coupled approaches. The time-periodic coupling method was found to offer an improved computational stability compared to the weakly-coupled approach. For the weak coupling method, convergence problems already arise for vessels with a length-to-radius ratio higher than 10, which for the time-periodic approach only occurs for vessels with a length-to-radius ratio above 60. These numbers (10, 60) are probably related to the wave length of the pressure wave. Decreasing the step size of the temporal discretisation from 0.01 to 0.001 s did not result in an improvement with respect to the computational stability. Since in this study, a quasi-stationary approach is applied for modelling the solid, added mass instabilities are not believed to be responsible for the convergence problems in the weakly-coupled approach. More likely, phase errors in the wall motion estimate are. For vessels with a length-to-radius ratio above 60, no convergence is achieved, both for decoupled and time-periodic approaches. Additional simulations, involving only an isolated solid domain, have shown

that the non-convergence is occurring in the solid calculation itself and is not a result of coupling issues. Although this non-convergence is odd, and should be solved, it is of minor relevance for this study, since for *in vivo* application, the simulation of vessels with a length-to-radius ratio ranging between 10 and 50 is of interest. Due to bifurcating and tapering, straight vessels with a higher length-to-radius ratio are hardly present; therefore, we believe that the simulation of these kind of geometries is not very relevant.

Both the decoupled and time-periodic coupled methods are successfully applied to geometries with a high length-to-radius ratio. The computations show that differences in solution between decoupled and time-periodic approach increase for geometries with increasing length-to-radius ratio. The differences are probably caused by the fact that for 1-D and 3-D models different material properties and geometry are applied for calculating the wall motion, resulting in differences in wall distension. This will have the most notable effects in vessels of high length-to-radius ratio.

For high length-to-radius geometries, the SCAFSI method, as introduced by Tezduyar et al. (2008a, b), probably also improves convergence properties, since the proposed time-periodic method and the SCAFSI method have similarities. A common step in both methods is that for the initial iteration, the wall motion is driven by a reference pressure signal. However, in the SCAFSI algorithm, this reference pressure is assumed spatially constant, whereas in the time-periodic approach, the reference pressure is determined from a 1-D wave propagation model. The 1-D pressure distribution is a more accurate approximation for the pressure distribution inside 3-D geometries than a constant pressure, especially for geometries with a high length/radius ratio. Test computations performed using the SCAFSI method on cerebral and abdominal aortic aneurysm geometries show improved convergence properties, without requiring a significant increase in computational demand. However, no results are shown for geometries with a high length-to-radius ratio, which is the focus of this study.

For the FSI-computations performed on the bifurcating geometry, no significant differences arise for the different coupling methods, which indicates that the change of pressure distribution on the vessel wall due to the 3-D flow phenomena is too small to significantly influence the vessel wall motion. Also, for the curved vessel, the differences observed are probably more a result of the high length-to-radius ratio, than of the 3-D flow phenomena due to the curvature. Consequently, it can be concluded that the advantage of the time-period coupling method with respect to the decoupled method will primarily show for geometries with a high length-to-radius ratio.

6. Conclusion

The time-periodic weakly coupled method presented in this study enables the modelling of FSI in long compliant vessels. This is a problem for weakly coupled methods based on timestep-wise coupling. Flow through straight compliant vessels with a length up to 60 times the radius is modelled successfully, whereas weakly coupled methods based on timestep-wise coupling only permit a length-to-radius ratio of 10. The simulations presented in this study show that the time-periodic method can be a valuable tool in the simulation of blood flow in arteries.

Acknowledgement

This work is part of and was supported by EUREKA Project E!3399 ART.MED, IS042015.

References

Bessems, D., Giannopapa, C.G., Rutten, M.C.M., van de Vosse, F.N., 2008. Experimental validation of a time-domain based wave propagation model of blood flow in viscoelastic vessels. Journal of Biomechanics 41 (2), 284–291.

Bessems, D., Rutten, M.C.M., van de Vosse, F.N., 2007. A wave propagation model of blood flow in large vessels using an approximate velocity profile function. Journal of Fluid Mechanics 580, 145–168.

Causin, P., Gerbeau, J.F., Nobile, F., 2005. Added-mass effect in the design of partitioned algorithms for fluid-structure problems. Computer Methods in Applied Mechanics and Engineering 194, 4506–4527.

de Hart, J., Peters, G.W.M., Schreurs, P.J.G., Baaijens, F.P.T., 2003. A three-dimensional computational analysis of fluid-structure interaction in the aortic valve. Journal of Biomechanics 36 (1), 103–112.

Dean, W.R., 1928. The streamline motion of fluid in a curved pipe. Philosophical Magazine and Journal of Science 5 (30), 673–695.

Deparis, S., Discacciati, M., Fourestey, G., Quarteroni, A., 2006. Fluid-structure algorithms based on Steklov–Poincaré operators. Computer Methods in Applied Mechanics and Engineering 195, 5797–5812.

Donea, J., Giuliana, S., Halleux, J.P., 1982. An arbitrary Lagrangian–Eulerian finite element method for transient dynamic fluid-structure interactions. Computer Methods in Applied Mechanics and Engineering 33, 689–723.

Fernandez, M.A., Gerbeau, J.F., Grandmont, C., 2006. A projection algorithm for fluid-structure interaction problems with strong added-mass effect. Comptes-Rendus de l'Académie des Sciences Paris. 342, 279–284.

Fernandez, M.A., Millisic, V., Quarteroni, A., 2005. Analysis of a geometrical multiscale blood flow model based on the coupling of ODEs and hyperbolic PDEs. Multiscale Modeling and Simulation 4, 215–236.

Fernandez, M.A., Moubachir, M., 2005. A Newton method using exact Jacobians for solving fluid-structure coupling. Computers and Structures 83, 127–142.

Formaggia, L., Gerbeau, J.F., Nobile, F., Quarteroni, A., 2001. On the coupling of 3d and 1d Navier–Stokes equations for flow problems in compliant vessels. Computer Methods in Applied Mechanics and Engineering 191, 561–582.

Formaggia, L., Nobile, F., Quarteroni, A., Veneziani, A., 1999. Multiscale modelling of the circulatory system: a preliminary analysis. Computing and Visualization in Science 2, 75–83.

Forster, C., Wall, W.A., Ramm, E., 2007. Artificial added mass instabilities in sequential staggered coupling of nonlinear structures and incompressible viscous flows. Computer Methods in Applied Mechanics and Engineering 196, 1278–1293.

Giannopapa, C.G., 2004. Fluid structure interaction in flexible vessels. Ph.D. Thesis, King's College London.

Gijsen, F.J.H., van de Vosse, F.N., Janssen, J.D., 1999a. Influence of the non-Newtonian properties of blood on the flow in large arteries: steady flow in a carotid bifurcation model. Journal of Biomechanics 32 (6), 601–608.

Gijsen, F.J.H., van de Vosse, F.N., Janssen, J.D., 1999b. Influence of the non-Newtonian properties of blood on the flow in large arteries: unsteady flow in a 90 degree curved tube. Journal of Biomechanics 32 (7), 705–713.

Hughes, T.J.R., Lubliner, J., 1973. On the one-dimensional theory of blood flow in large vessels. Mathematical Biosciences 18, 161–170.

Ku, D.N., 1983. Hemodynamics and atherogenesis at the human carotid bifurcation. Ph.D. Thesis, Georgia Institute of Technology.

Matthies, H.G., Steindorf, J., 2002. Partitioned but strongly coupled iteration schemes for nonlinear fluid-structure interaction. Computers and Structures 80, 27–30.

Milnor, W.R., 1989. Hemodynamics. Williams & Wilkins.

Olufsen, M.S., Pesking, C.S., Kim, W.Y., Pedersen, E.M., Nadim, A., Larsen, J., 2000. Numerical simulation and experimental validation of blood flow in arteries with structured-tree outflow conditions. Annals of Biomedical Engineering 28, 1281–1299.

Quarteroni, A., Veneziani, A., 2003. Analysis of a geometrical multiscale model based on the coupling of ODEs and PDEs for blood flow simulations. Multiscale Modeling and Simulation 1, 173–195.

Reuderink, P.J., van de Vosse, F.N., van Steenhoven, A.A., van Dongen, M.E.H., Janssen, J.D., 1993. Incompressible low-speed-ratio flow in non-uniform distensible tubes. International Journal for Numerical Methods in Fluids 16, 597–612.

Rutten, M.C.M., 1998. Fluid–solid interaction in large arteries. Ph.D. Thesis, Eindhoven University of Technology.

Segal, A., 2004. SEPRAN introduction, user's manual, programmer's guide and standard problems. Ingenieursbureau SEPRA.

Stergiopulos, N., Westerhof, B.E., Westerhof, N., 1999. Total arterial inertance as the fourth element of the Windkessel model. American Journal of Physics 45, H81–H88.

Taylor, C.A., Hughes, T.J.R., Zarins, C., 1996. Computational investigations in vascular disease. Computational Physics 10, 224–232.

Taylor, C.A., Hughes, T.J.R., Zarins, C.K., 1998. Finite element modelling of blood flow in arteries. Computer Methods in Applied Mechanics and Engineering 158, 155–196.

Tezduyar, T.E., Sathe, S., Schwaab, M., Conklin, B.S., 2008a. Arterial fluid mechanics modeling with the stabilized space-time fluid-structure interaction technique. International Journal for Numerical Methods in Fluids 57 (5), 601–629.

Tezduyar, T.E., Schwaab, M., Sathe, S., 2008b. Sequentially-coupled fluid-structure interaction (SCAFSI) technique. Computer Methods in Applied Mechanics and Engineering July 2008, DOI: 10.1016/j.cma.2008.05.024, (published online).

Tortoli, P., Michelassi, V., Bambi, G., Guidi, F., Righi, D., 2003. Interaction between secondary velocities, flow pulsation and vessel morphology in the common carotid artery. Ultrasound in Medicine and Biology 29 (3), 407–415.

van de Vosse, F.N., de Hart, J., van Oijen, C.H.G.A., Bessems, D., Gunther, T.W.M., Segal, A., Wolters, B.J.B.M., Stijnen, J.M.A., Baaijens, F.P.T., 2003. Finite-element-based computational methods for cardiovascular fluid-structure interaction. Journal of Engineering Mathematics 47 (3–4), 335–368.

van Loon, R., Anderson, P.D., de Hart, J., Baaijens, F.P.T., 2004. A combined fictitious domain/adaptive meshing method for fluid-structure interaction in hear valves. International Journal of Numerical Methods in Fluids 46, 533–544.

Vignon-Clementel, I.E., Figueroa, C.A., Jansen, K.E., Taylor, C.A., 2006. Outflow boundary conditions for three-dimensional finite element modeling of blood flow and pressure in arteries. Computer Methods in Applied Mechanics and Engineering 195, 3776–3796.

Wolters, B.J.B.M., Rutten, M.C.M., Schurink, G.W.H., Kose, U., de Hart, J., van de Vosse, F.N., 2005. A patient-specific computational model of fluid-structure interaction in abdominal aortic aneurysms. Medical Engineering and Physics 27, 871–883.